SCIENCE CHINA
Physics, Mechanics & Astronomy

•**Article**•

April 2021 Vol. 64 No. 4: 244711
https://doi.org/10.1007/s11433-020-1654-4

Suspended penetration wetting state of droplets on microstructured surfaces

Jing Lou[1], SongLin Shi[1], Chen Ma[1], CunJing Lv[1*], and QuanShui Zheng[1,2*]

[1] *Department of Engineering Mechanics and Center for Nano and Micro Mechanics, Tsinghua University, Beijing 100084, China;*
[2] *State Key Laboratory of Tribology, Tsinghua University, Beijing 100084, China*

Received September 14, 2020; accepted December 24, 2020; published online February 23, 2021

When a water droplet on a micropillar-structured hydrophobic surface is submitted to gradually increased pressure, the Cassie-Baxter wetting state transforms into the Wenzel wetting state once the pressure exceeds a critical value. It has been assumed that the reverse transition (Wenzel-to-Cassie-Baxter wetting state) cannot happen spontaneously after the pressure has been removed. In this paper, we report a new wetting-state transition. When external pressure is exerted on a droplet in the Cassie-Baxter wetting state on textured surfaces with high micropillars to trigger the breakdown of this wetting state, the droplet penetrates the micropillars but does not touch the base of the surface to trigger the occurrence of the Wenzel wetting state. We have named this state the suspended penetration wetting state. Spontaneous recovery from the suspended penetration wetting state to the initial Cassie-Baxter wetting state is achieved when the pressure is removed. Based on the experimental results, we built models to establish the penetration depth that the suspended penetration wetting state could achieve and to understand the energy barrier that influences the equilibrium position of the liquid surface. These results deepen our understanding of wetting states on rough surfaces subjected to external disturbances and shed new light on the design of superhydrophobic materials with a robust wetting stability.

wetting, micropillars, hydrophobic, transition, stability

PACS number(s): 47.55.D-, 47.55.Np, 68.08.-P, 68.03.Cd, 68.08.Bc

---

Citation: J. Lou, S. L. Shi, C. Ma, C. J. Lv, and Q. S. Zheng, Suspended penetration wetting state of droplets on microstructured surfaces, Sci. China-Phys. Mech. Astron. **64**, 244711 (2021), https://doi.org/10.1007/s11433-020-1654-4

---

1 Introduction

Superhydrophobic surfaces display spectacular properties, such as self-cleaning [1-4], water repellency [5,6], highly efficient condensation [7-9], and anti-icing [10-12]. These properties mostly stem from the hydrophobic coating and micro-/nanostructures on the substrate, which can trap air between the water and the base of the surface, enabling the water to remain suspended over the structures with just an ultra-small solid-liquid contact region, leading to a Cassie-Baxter wetting state. However, when subjected to external disturbances, such as mechanical vibration [13,14], evaporation [15], drop impact [16], and exerted pressure [17-19], water may readily penetrate the surface textures, transforming into an irreversible Wenzel wetting state [6,19]. Once a droplet is in the Wenzel wetting state, water affinity with the textures is significantly increased, resulting in the failure of the superhydrophobicity and its unique functions. Finding ways to avoid the irreversible breakdown of the Cassie-Baxter wetting state and enhance the robustness of the superhydrophobicity is challenging, but it merits further theoretical and experimental attention.

---

*Corresponding authors (CunJing Lv, email: cunjinglv@tsinghua.edu.cn; QuanShui Zheng, email: zhengqs@tsinghua.edu.cn)

Over the past decade, in order to realize a wetting-state transition from the Wenzel wetting state to the Cassie-Baxter wetting state, researchers have employed various methods, such as electric [20,21] and thermal techniques [20], mechanical vibration [22-25], and condensation [26]. Through the use of condensation, Dorrer and Rühe [26] achieved a Wenzel-to-Cassie-Baxter (W2C) wetting-state transition in which the contact-line pinning was overcome due to the dynamic force resulting from the decrease in surface energy after the coalescence of the droplets. Krupenkin et al. [20] realized reversible transitions between the Cassie-Baxter and the Wenzel wetting states through the application of an electrical voltage and current to produce a momentary evaporation of a microscopically thin layer of liquid immediately adjacent to the substrate surface. Boreyko and Chen [22] firstly demonstrated that a mechanical vibration can be employed to overcome the energy barrier during the transition from the sticky Wenzel wetting state to the non-sticking Cassie-Baxter wetting state. Boreyko et al. [22-24] have also provided the criteria for the reversible transition in relation to the topology of the substrates and their wettability. However, all these methods need an external energy input or require complicated techniques, so they are not suited to a broad range of practical applications. However, researchers have pursued a fundamental understanding of the underlying mechanism behind the stability of superhydrophobic surfaces and have devoted their efforts to promoting its robustness from the source. Very recently, by minimizing hydrophobic conical structures to nanosized, Mouterde et al. [27] achieved a high antifogging efficiency close to unity and water departure of droplets smaller than 2 µm. Li et al. [28] developed a method for a spontaneous W2C transition and named the property identified in this transition the monostability. They also demonstrated that there exists a region in the parameter space composed of the texture geometry and the contact angle in which the monostability can be maintained. However, although the monostability was attained on one-tier microstructured surfaces for mercury, it was only attained on two-tier nano-/microstructured surfaces for water. In many practical applications, especially in antifogging, droplets with a much smaller scale compared with the scale of the roughness of the textures will be formed in the very initial stage of condensation. In this case, the small droplets will first come into contact with the one-tier surface. After that, whether monostability can be attained on a one-tier surface or not is important, as it determines whether the droplets will further evolve into a Wenzel wetting state or a Cassie-Baxter wetting state. Until now, how to achieve monostability on one-tier surfaces has remained a challenge. In this paper, by carrying out experiments on one-tier micropillars, we not only pursue a further understanding of the interactions between droplets and hydrophobic textures, but also aim to promote the robustness of the hydrophobicity, which are central to the emerging applications of superhydrophobic materials, such as self-cleaning, anti-icing, and water harvesting.

Our results show that when we exert pressure on small droplets on one-tier textured hydrophobic substrates with very high micropillars, even though the Cassie-Baxter wetting state is destroyed, a subsequent suspended penetration wetting state is formed that stops the wetting state from breaking down further to the sticky Wenzel wetting state. When the external pressure is released, the three-phase contact lines in the micropillars retreat and the initial Cassie-Baxter wetting state, surprisingly, recovers. In contrast to the known Wenzel and Cassie-Baxter wetting states [29,30], the double-roughness structure wetting modes [17] and the penetration regimes [31], the wetting behaviors we have observed suggest a novel wetting state transition. The wetting behaviors reported in this study may provide a promising solution for overcoming the fragile wetting-state transition on one-tier micropillared substrates.

2 Experiments

Preparation of the microstructures. As shown in Figure 1(a),

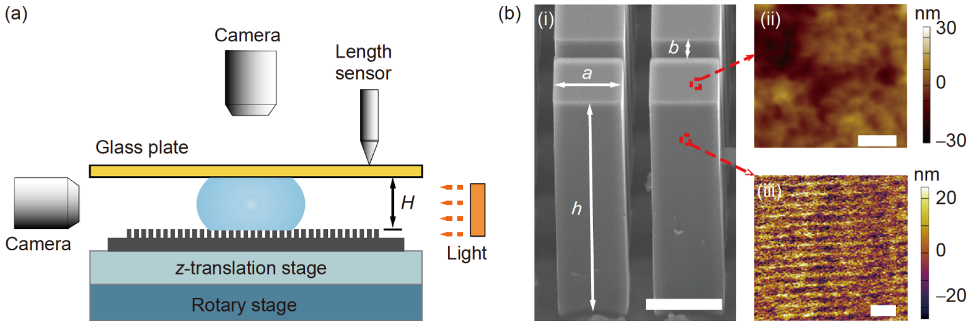

Figure 1 (Color online) Schematic of the experimental setup and the samples. (a) Main components of the experimental setup are shown from the side view. (b) (i) Scanning electron microscopy (SEM) image of the micropillars, with the corresponding width a=18 µm, spacing b=12 µm, and height h=80 µm. The scale bar is 20 µm. (ii) Atomic force microscopy (AFM) image showing the roughness of a region on the top of a single pillar; the roughness is 8 nm, and the scale bar is 500 nm. (iii) AFM image showing the roughness of a region on the side wall of a single pillar; the roughness is 12 nm, and the scale bar is 1 µm.

there are two stages involved in the study of the wetting behaviors; we first pressed a droplet using a glass plate against a micropillar-structured substrate, and then we lifted the glass plate to check the reaction of the droplet. To decrease the adhesion between the droplet and the glass plate, the glass plate was treated with a commercial coating (Glaco, Soft99) using the methods described previously [32,33]. The resulting receding and advancing contact angles were θ_{gr}=160°±2° and θ_{ga}=170°±2°, respectively. We tested two sets of 1 cm×1 cm micropillared substrates on a silicon wafer fabricated using photolithography. Each pillar was square-shaped and square-distributed, as indicated in Figure 1(b), and the height of the pillars was maintained at h=80 μm. In Set I, the side length of the pillars was maintained at a= 8.3 μm, but spacing b was varied from 5 to 25 μm. Based on these geometrical parameters, we obtained a different area fraction $f=a^2/(a+b)^2$ ranging from 0.06 to 0.4 and a roughness $r=1+4ah/(a+b)^2$ ranging from 3.4 to 16. In Set II, the micropillar structures had the same area fraction values as Set I but with a fixed side length a=18.7 μm. Thus, the range of the roughness became $r\in[2.1,\ 7.7]$. In order to achieve hydrophobicity, the substrates were coated with a layer of 1*H*, 1*H*,2*H*,2*H*-perfluorodecyltrichlorosilane ($CF_3(CF_2)_7(CH_2)_2$-$SiCl_3$, FDTS) precursor molecules using the CVD method in a vacuum environment [34]. On the flat silicon FDTS-coated wafer, the Young contact angle was θ_0=110°±2°. The advancing and receding contact angles were obtained by slowly moving a water droplet horizontally at the speed of 10 μm/s [28]. After measuring the angles around the front and rear three-phase contact lines, we obtained θ_a=118°±2° and θ_r=98°±2°, respectively.

In order to record the vertical displacement of the glass plate, a length sensor (Heidenhain-Metro 2581) was first attached to the superhydrophobic glass plate; thus, its initial position (i.e., the reference zero point) was calibrated. Then, by mounting the glass plate to a motorized z-translation stage, we exerted a vertical displacement on the glass plate to compress the droplet. The real-time separation H (Figure 1(a)) between the glass plate and the substrate was easily calculated using the output data of the length sensor. To obtain the transverse section area A (Figure 2) of the confined droplet, the appearance of the droplet was captured from above using a commercial CCD camera (Canon 550D, Hi-Scope advanced KH3000). In this experiment, considering that the droplet was tightly confined, like a pancake, and H was much smaller than its transverse scale, before the water droplet penetrated the micropillars, we estimated the volume V of the droplet in terms of an approximation $V\approx AH$. In addition, a humidifier was employed to compensate the loss of water due to evaporation. In other words, we assumed that the volume of the droplet was constant during the whole experimental process.

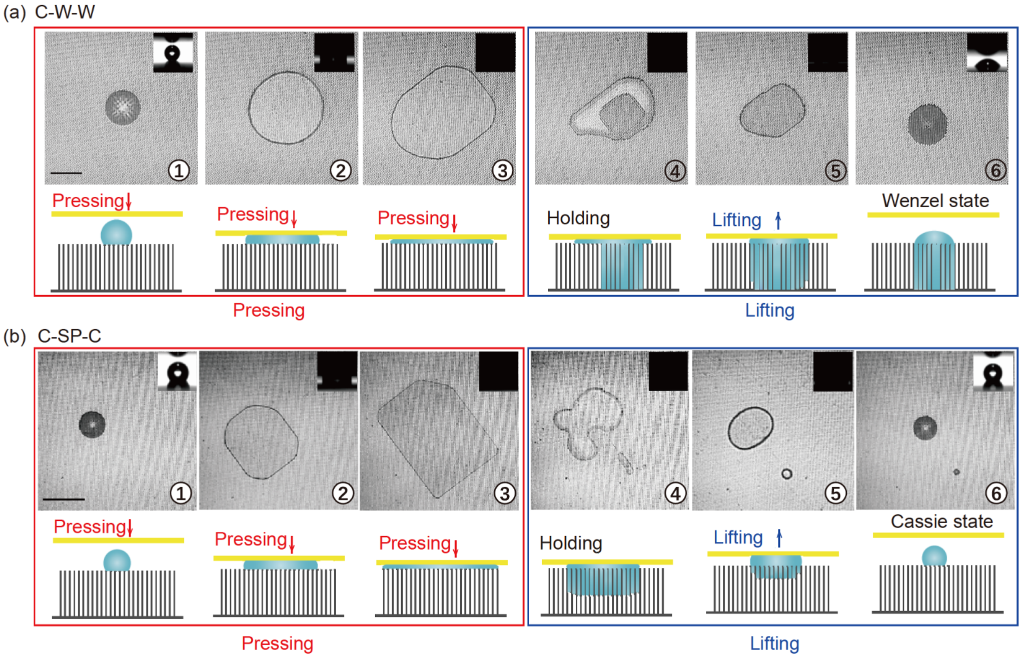

Figure 2 (Color online) Experimental observation and the corresponding frames. (a) Snapshots of a water droplet pressed against the FDTS-treated micropillared substrates. The solid-liquid area fraction is f=0.172, and the volume of the droplet is 40 nL. The droplet in the Cassie-Baxter wetting state (circle 1) is squeezed (circles 2 and 3) until it partially (circle 4) and completely (circle 5) penetrates the micropillars. After holding the glass plate in this position for about 2 s, it is lifted, leaving a droplet in the Wenzel wetting state (circle 6). (b) The same experimental processes but with f=0.56 and V=17 nL. When the droplet (circle 1) is sufficiently compressed (circles 2 and 3), it suddenly penetrates the pillars (circle 4) but without touching the base of the substrate. On lifting (circle 5), the droplet eventually reverses to the initial Cassie-Baxter wetting state (circle 6). The insets show the corresponding processes from a side view. The scale bars represent 500 μm.

3 Results and discussion

3.1 Pressing and lifting processes

As shown in Figure 2, we first provide comparisons between a typical case of an irreversible wetting transition (Figure 2(a)) and the exceptional wetting behaviors we observed in this study (Figure 2(b)). In Figure 2(a), the geometrical parameters of the micropillars are a=8.3 μm, b=11.7 μm, and h=80 μm, and the corresponding area fraction and roughness are f=0.172 and r=7.64, respectively. A small droplet was produced using a syringe and was then deposited on the substrate. The measured Cassie-Baxter contact angle and the radius of the droplet were $\theta^*\approx140°$ and $R\approx215$ μm, respectively (as shown in the inset of circle 1, Figure 2(a)). Based on these values, the volume of the droplet was calculated using $V=\pi R^3(1-\cos\theta^*)^2(2+\cos\theta^*)/3$ and resulting in $V\approx40$ nL. As the glass plate was mounted on a motorized z-translation stage, the z-position of the plate could be precisely controlled. In order to guarantee a quasi-static process, the z-position of the glass plate was decreased at a speed of $\mathrm{d}H/\mathrm{d}t=-2$ μm/s. We observed that, in this stage, the droplet was pressed smoothly into a pancake shape (see circles 2 and 3, Figure 2(a)). In circle 4 of Figure 2(a), we can see that when H reached a critical value H_{cr}, a sudden penetration transition was triggered (which was observed by the variation in the visualization of the appearance of the liquid, as seen from above). The dark square region corresponds to the contact with the base of the structure, forming a local Wenzel wetting state. From then, the z-position of the glass plate was further decreased until the glass plate touched the sample (circle 5). After holding the plate in this position for about 2 s, we reversed the glass plate's direction of movement while maintaining the speed at $\mathrm{d}H/\mathrm{d}t=2$ μm/s. After the glass plate was lifted until it was high enough to detach from the droplet, the droplet remained in a spherical shape with a much lower contact angle (≈50°, see circle 6, Figure 2), suggesting a Wenzel wetting state. We call this the typical Cassie-Wenzel (C-W) wetting-state transition [35].

As shown in Figure 2(b), when micropillars that are much denser (i.e., a=18.7 μm, h=80 μm, b=6.3 μm, f=0.56, and r=10.57) were used, a different scenario to that shown in Figure 2(a) was presented. In this case, the volume and size of the droplet were V=17 nL and R=170 μm, respectively. When the droplet was deposited on this surface, the Cassie-Baxter contact angle was 120°±1°, appreciably lower than the value in Figure 2(a), due to an increase in the area fraction f. When the droplet was quasi-statically compressed, it first adopted a pancake shape, but the boundary of the liquid gradually deviated from this shape (circle 2). With further compression, this deviation developed, and the transverse area evolved to a square (circle 3). When the distance H reached the critical value H_{cr}, a sudden breakdown of the Cassie-Baxter wetting state was observed (circle 4). Meanwhile, a small satellite droplet was ejected from the main droplet. At this point, we stopped running the z-translation stage and held the plate in this position for about 2 s. We then carefully decreased H to a minimum value until the plate touched the top of the micropillars. After that, we lifted the glass plate, and the liquid started to retreat (circle 5). With further lifting, the liquid left the micropillars, and we finally observed that the droplet was restored to a spherical shape (circle 6) with a contact angle of 124°±1°, which was very close to the initial contact angle. This means that the droplet completely recovered to the initial Cassie-Baxter wetting state after a loading-unloading process. Based on these wetting behaviors, it is reasonable for us to postulate that in circles 4 and 5 of the processes described above, the liquid surface at the bottom of the droplet was suspended among the micropillars and did not touch the substrate, so we have named this wetting state the suspended penetration (SP) wetting state. Furthermore, this phenomenon (C-SP-C transition) is different from all the previous reported wetting transitions, such as the irreversible C-W wetting-state transition [18,29,30], the Wenzel-Cassie-Baxter (W-C) intermediate wetting state [17,36], and the monostable CWC wetting state transitions [28].

As mentioned above, when the droplet was pressed into the SP wetting state, we could not directly observe the solid-liquid contact region in detail from the side view because of the narrow spacing of the pillars. Since the apparent area of the compressed droplet suddenly shrank from circle 3 to 4 (Figure 2(b)), the conservation of the liquid volume required that the droplet must have penetrated the pillars. In addition, the appearance of the water "pancakes" at circles 3, 4, and 5 in Figure 2(b), as viewed from above, suggests that the values of the grayscale were quite homogeneous inside the boundary of the droplet, so we can reasonably assume that the thicknesses of the pancakes were uniform except for the regions close to the boundary. Macroscopically, the liquid interface at the bottom of the droplet might be nearly "flat". Here, by combining the constant volume V, the transverse section area A of the liquid as viewed from above, and the experimentally recorded height H, we estimated the average penetration depth Z by employing the following relationship:

$$V = AH + A(1-f)Z, \tag{1}$$

where $V_1=AH$ is an approximation of the liquid volume between the glass plate and the top of the pillars, and $V_2=A(1-f)Z$ is an approximation of the suspended liquid volume that is confined between the pillars. Since the volume V and the area fraction f are known in advance, and H and A can be measured during the experimental process, the penetration depth Z can be calculated in terms of eq. (1).

In the relationships demonstrated in Figure 3, we use red and blue dots to denote the pressing (squeezing) and lifting (releasing) processes of the glass plate, respectively. The

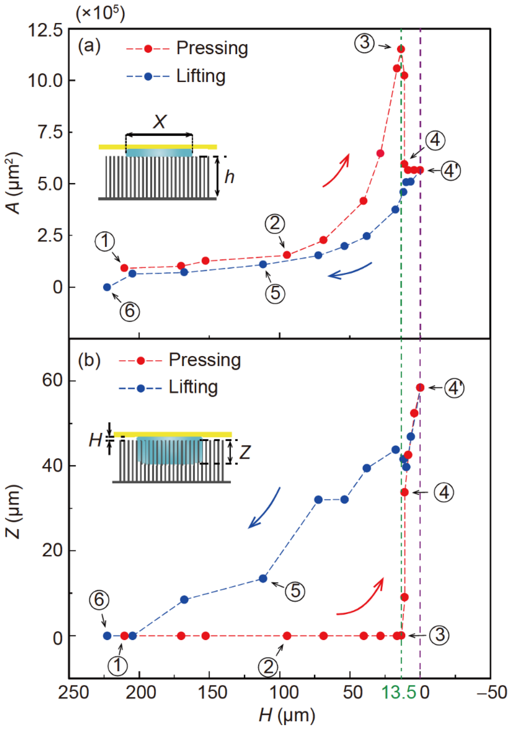

Figure 3 (Color online) Transverse area A and penetration depth Z of the liquid during one period of pressing (red circles) and lifting (blue circles). (a) The relationship between A and H. (b) The relationship between Z and H. The circled numbers correspond to the different stages shown in Figure 2(b), among which the appearance of the droplet marked as circle 4′ is similar to that of circle 4. The associated arrows denote the direction of movement of the processes.

processes marked using circled numbers correspond to the stages shown in Figure 2(b). As shown in Figure 3(a), when the droplet was being pressed (i.e., H was decreasing), the transverse area A increased gradually and there was no penetration. However, when the critical value of H was reached, i.e., H_{cr}=13.5 μm (see circle 3), based on the variation of the value of the grayscale of the liquid pancake, the liquid surface at the bottom of the droplet suddenly penetrated the micropillars and, at the same time, transformed from a square-shaped pancake into an irregular shape. As shown in Figure 3(a), the transition (from circle 3 to 4) induced a sudden decrease (~43%) in the pancake area A. We then held the plate in position for about 2 s and then pressed the droplet a little more so that the glass plate reached a minimum height, i.e., $H\approx0$ μm (see circle 4′ in Figure 3(a)). Since the appearance of the droplet represented by circle 4′ was very similar to that of circle 4, we have not listed frame 4′ in Figure 2(b). At this point, with the measured value $A\approx5.5\times10^5$ μm^2 and using eq. (1), we were able to calculate the penetration depth $Z\approx60$ μm (see frame 4′ in Figure 3(b)), which was notably smaller than the height of the micropillars (h=80 μm). This indicates that, during the transition, even though the liquid surface at the bottom of the droplet penetrated the micropillars, the droplet did not touch the substrate (see the sketched inset in Figure 3(b)), and it therefore stayed in an SP wetting state, as mentioned above.

After that, we lifted the glass plate. When the value of H was gradually increased, both A and Z continuously decreased until their values almost returned to their initial values (see circles 1 and 6 in Figure 3(a) and (b)). These processes indicate that after a period of squeezing and releasing, the wetting state of the droplet recovers to the initial Cassie-Baxter wetting state. This wetting behavior benefits the robustness and the stability of the hydrophobicity of the textures because the occurrence of a complete wetting state (i.e., the Wenzel wetting state) is avoided. We have carried out systematic tests on these two sets of micropillared substrates, however, the SP wetting state could only be realized in a few samples (more details about the parameters are given in Table 1). Moreover, it has been challenging for us to recreate droplets of the same volume, so the experimental

Table 1 Details of the parameters for the SP wetting state. S, f, V, and H are experimentally measured values. Z represents the calculated values from eq. (1), based on the measured values of H and A. Z_{t1} and Z_{t2} represent the theoretical values obtained by employing the Lagrange multiplier method and by considering the energy barrier from eq. (8), respectively

Sample	S (μm)	f	V (nL)	H (μm)	Z (μm)	Z_{t1} (μm)	Z_{t2} (μm)
1	4.675	0.56	17	8.6	42.6	133	31
2	4.675	0.56	19	9.7	37.8	93	12
3	4.35	0.44	22	8.9	58	199	76
4	4.35	0.44	22	10.9	50.0	165	57
5	4.35	0.44	22	9.9	56.0	182	67
6	4.35	0.44	23.2	11.6	50	155	51
7	4.35	0.44	25.2	12.2	60	149	47
8	4.35	0.44	22.5	13.9	11	109	25
9	4.35	0.44	22.5	12.9	19	129	37
10	4.35	0.44	10.3	7.2	58	173	67
11	2.05	0.3	6.2	7.2	41	111	51
12	2.11	0.28	30.5	12.7	65	129	46
13	2.11	0.28	30.5	11.7	66	143	58

data in Figure 3(a) and (b) represents a single test.

3.2 Theoretical analyses

We now try to establish the geometrical configuration of the droplet when it is in the SP wetting state. To realize this aim, we built models based on theoretical analyses of the surface energy E of the droplet. For any given system, the liquid will adopt a configuration with the minimum surface energy. To find this configuration, we must first establish the components of the surface energy E.

As shown in Figure 4, the surface energy of the droplet is formed from the solid-liquid and liquid-vapor interfaces. The solid-liquid interfaces consist of three parts (marked in Figure 4(a) and (b) using blue lines): (1) the interface between water and the glass plate, for which the surface energy can be written as $A(\gamma_{SL}{}^{g}-\gamma_{SV}{}^{g})=-A\gamma_{LV}\cos\theta_{g0}$, where γ_{LV}, $\gamma_{SL}{}^{g}$, and $\gamma_{SV}{}^{g}$ represent the liquid-vapor, glass-liquid, and glass-vapor interfacial tensions, respectively, and θ_{g0} is the contact angle of the water on the glass plate; (2) the interfaces between the water and the top of the micropillars, for which the surface energy can be written as $Af(\gamma_{SL}-\gamma_{SV})=-Af\gamma_{LV}\cos\theta_0$, where γ_{SL} and γ_{SV} represent the FDTS-coated silicon-liquid and silicon-vapor interfacial tensions, respectively, and θ_0 is the intrinsic contact angle of the water on the FDTS-coated silicon wafer. As, during the droplet's collapse, the liquid penetrates between the micropillars, we adopted the receding contact angles θ_{gr} (θ_{gr}=160°±2°) and θ_r (θ_r=98°±2°) instead of θ_{g0} and θ_0, respectively; (3) the interfaces between the water and the sides of the micropillars (see blue lines in Figure 4(b)), for which the corresponding surface energy is $(AZf/S)(\gamma_{SL}-\gamma_{SV})=-(AZf/S)\gamma_{LV}\cos\theta_0$, where S is the ratio between the area and the perimeter of a single micropillar. Since the micropillars are square, $S=a/4$. Moreover, f/S refers to the length of the solid-liquid contact-line per unit area of the bottom of the droplet. As, during the collapse, the liquid fingers penetrate between the pillars, we used the advancing contact angle θ_a (θ_a=118°±2°) instead of θ_0. The remaining surface energy results from the liquid-vapor interface, which also consists of three parts (see the red curves in Figure 4(a) and (b)): (1) the torus-shaped interface between the glass plate and the top of the micropillars, for which the surface energy is $c_1LH\gamma_{LV}$, where L is the perimeter of the liquid as seen from above; (2) the liquid interface of the bottom of the droplet extending into the micropillars, for which the corresponding surface energy is $c_2A(1-f)\gamma_{LV}$; and (3) the interface of the fingers on the side of the penetrated liquid, for which the surface energy is $c_3LZ(1-f^{1/2})\gamma_{LV}$. The coefficients employed to correct the estimates of the areas of the curved surfaces were c_1, c_2, and c_3, which rely on the minimization of the surface energy.

Based on the above definitions, we obtained eq. (2):

$$
\begin{aligned}
\frac{E}{\gamma_{\mathrm{LV}}} &= -A\cos\theta_{\mathrm{gr}} - Af\cos\theta_{\mathrm{r}} - \frac{AZf}{S}\cos\theta_a + c_1LH \\
&\quad + c_2A(1-f) + c_3LZ\left(1-\sqrt{f}\right) \\
&= \left[c_2(1-f) - \cos\theta_{\mathrm{gr}} - f\cos\theta_{\mathrm{r}} - \frac{4Zf}{a}\cos\theta_a\right]X^2 \\
&\quad + 4\left[c_1H + c_3Z\left(1-\sqrt{f}\right)\right]X. \qquad (2)
\end{aligned}
$$

For the sake of simplicity, we assumed that the liquid was square, so we used $L=4X$ and $A=X^2$ in eq. (2). In order to determine the wetting state of the droplet, i.e., the unknown variables X and Z for the given values of V and H, we used the Lagrange multiplier method. We rewrote eqs. (1) and (2) as the following:

$$
\begin{aligned}
\frac{E^*}{\gamma_{\mathrm{LV}}} &= \left[c_2(1-f) - \cos\theta_{\mathrm{gr}} - f\cos\theta_{\mathrm{r}} - \frac{4Zf}{a}\cos\theta_a\right]X^2 \\
&\quad + 4\left[c_1H + c_3Z\left(1-\sqrt{f}\right)\right]X \\
&\quad + \lambda\left\{X^2[H+(1-f)Z] - V\right\}, \qquad (3)
\end{aligned}
$$

where λ is the Lagrange multiplier. As we know, for the given values of V and H, the system tends to evolve into a configuration with a minimum surface energy, which can be determined by eq. (4):

$$
\frac{\partial E^*}{\partial X} = 0,\ \frac{\partial E^*}{\partial Z} = 0,\ \frac{\partial E^*}{\partial \lambda} = 0. \qquad (4)
$$

The third equation in eq. (4) leads to eq. (1). A combination of the first two equations in eq. (4) will remove λ,

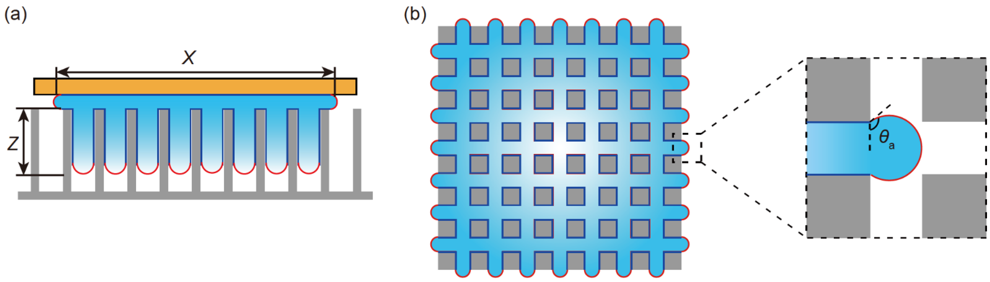

Figure 4 (Color online) Schematic of the droplet in the SP wetting state as viewed from the side (a) and from above (b). The solid-liquid and liquid-vapor interfaces are denoted using blue lines and red curves, respectively. In (b), details of the wetting state as seen from the side of the micropillars are shown enlarged.

leading to eq. (5):

$$Z=\frac{X}{2c_3\left(1-\sqrt{f}\right)}\cdot\left[-\cos\theta_{\mathrm{gr}}-f\cos\theta_{\mathrm{r}}+c_2(1-f)+\frac{4H}{a}\cdot\frac{f}{1-f}\cos\theta_{\mathrm{a}}\right]+\frac{H}{c_3}\cdot\left(\frac{c_1}{1-\sqrt{f}}-\frac{2c_3}{1-f}\right).\qquad(5)$$

For this experiment, f, θ_{gr}, θ_{r}, θ_{a}, and V were the given parameters. Consequently, for a given value of H, the other two unknown variables X and Z could be solely determined by employing eqs. (1) and (5).

Next, we provide the calculated results based on the above theory. For the sake of simplicity, we treated part (1) of the liquid-vapor interface as a half-torus in which $c_1\approx\pi/2$. Considering that part (2) of the liquid-vapor interface does not deform very much, $c_2\approx 1$. However, here we must emphasize that part (3) of the liquid-vapor interface should be approached with caution. After the collapse of the liquid (i.e., circles 3 and 4 in Figure 2(b)), the liquid fingers suddenly penetrated the micropillars, so the contact angle on the side wall of the micropillar (see the enlarged region in Figure 4(b)) reached the maximum. It is reasonable to use $\theta_{\mathrm{a}}=120°$, which allowed us to obtain $c_3=\theta_{\mathrm{a}}/\sin\theta_{\mathrm{a}}\approx 2.4$, which is, in other words, the ratio between the arc length (the red curve) and the spacing b. In Table 1, we provide the comparisons between the experimental and the theoretical results, in which S, f, and V are the given parameters, H is recorded by the length sensor, and Z is the calculated value from eq. (1) based on the experimentally measured values of H and A. Z_{t1} is the value obtained from our model (i.e., eqs. (1)-(5)) with the known values V and the measured value H. The comparisons of the sample results indicate that most of the theoretical values of Z_{t1} are larger than the experimentally measured Z. These large gaps may result from some uncertainties, such as the contact-line pinning and the dissipation of the volume of the droplet during the experiments.

In order to understand the gaps between the values obtained for Z and Z_{t1}, we conducted further analyses from a different viewpoint. First, eq. (1) leads to the relationship $A=V/[H+(1-f)Z]$, from which we obtained eq. (6) by substituting this relationship into eq. (2):

$$\frac{E}{\gamma_{\mathrm{LV}}}=\left[c_2(1-f)-\cos\theta_{\mathrm{gr}}-f\cos\theta_{\mathrm{r}}-\frac{4Zf}{a}\cos\theta_{\mathrm{a}}\right]\cdot\frac{V}{H+(1-f)Z}+4\left[c_1H+c_3Z\left(1-\sqrt{f}\right)\right]\cdot\sqrt{\frac{V}{H+(1-f)Z}}.\qquad(6)$$

The geometrical parameters V, f, θ_{gr}, θ_{r}, and θ_{a} and the coefficients c_1, c_2, and c_3, are known. When H is given, eq. (6) can give the variation of the surface energy E as the function of Z. In other words, for a fixed value of H, there must be a minimum surface energy, and the corresponding value Z corresponds to the equilibrium state of the droplet. For example, we chose the experimental value H=8.6 μm (see Sample 1 in Table 1), and then we checked the relationship between E/γ_{LV} and Z (Figure 5) obtained by eq. (6).

As shown in Figure 5, the blue point (133 μm) corresponds to the point with a minimum surface energy. In fact, the blue point is also the value of Z_{t1}=133 μm obtained by employing the Lagrange multiplier method (i.e., based on eqs. (1)-(5)). The red point (Z=42.6 μm) is the position that the liquid surface stops at in the real experiment. As shown in Table 1 for all the samples, the values for Z obtained by using eq. (1) were always smaller than the theoretical values for Z_{t1} obtained by using the Lagrange multiplier method. In other words, during compression, the liquid surface always stopped at a position before which the wetting state attained a minimum surface energy. This inconsistency indicates that, during the above analyses, we might have missed an influencing factor. Furthermore, Figure 5 suggests that the curve is quite flat when the surface energy reaches its minimum value (blue dot), which indicates that, in the real experiment, even a small energy barrier would block the movement of the liquid-vapor menisci from reaching the equilibrium predicted by the theory, and this is the reason why the experimental value Z is always smaller than Z_{t1}. In the above analyses, we assumed that the transverse motion of the liquid in the micropillars (see Figure 4(b)), as well as the solid-liquid-vapor three-phase contact lines, was continuous. However, in the real process, even between two successive rows, the transverse movement of the menisci is not continuous but associated with wetting/dewetting processes from one row to the next of the pillar and the morphological transitions of the topology of the liquid. In this case, a considerable number of energy barriers have to be overcome and

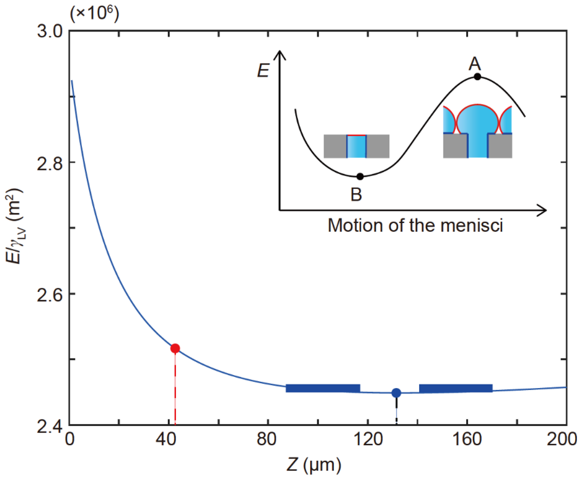

Figure 5 (Color online) Relationship between E/γ_{LV} and Z calculated using eq. (6) and the parameters of Sample 1. The blue point represents the solution of eq. (6) with the minimum surface energy. The red point represents the stagnation point of the liquid surface in the experiment. The inset illustrates the energy barrier during the transition process, and points A and B correspond to the two quasi-static wetting states during the transition.

should be taken into consideration. For the sake of simplicity, we assumed that the energy barrier was related to the area of the menisci on each side of the square-shaped liquid that penetrated the gap between the micropillars, which was proportional to XZ (as there were four sides, $4XZ$). Then, we approximated the energy barrier ΔE as:

$$\frac{\Delta E}{\gamma_{\mathrm{LV}}} = 4\alpha XZ, \tag{7}$$

where α is a coefficient to correct the uncertainty of the energy barrier. As shown in the inset of Figure 5 (corresponding to the red curves in Figure 4(b)), two wetting states during the transverse motion of the liquid menisci that penetrates the gap between the micropillars are demonstrated using schematics, and points A and B in the curve represent the corresponding surface energy. E_{A} represents the wetting state as far as the liquid-vapor menisci extends before coalescing, and E_{B} represents the wetting state that allows the liquid-vapor menisci to pin to the edges of the micropillars. The energy barrier between A and B can be expressed as $\Delta E = E_{\mathrm{A}} - E_{\mathrm{B}}$, where E_{A} and E_{B} are approximately written as $4XZ(2\pi/3)\gamma_{\mathrm{LV}}$ (taking the contact angle as about 120° on the sides of the micropillars) and $4XZ(1-f^{1/2})\gamma_{\mathrm{LV}}$, respectively, suggesting $\alpha \approx 2\pi/3-1+f^{1/2}$.

During compression, the liquid surface reaches a balance point if the following relationship is satisfied:

$$-\frac{\mathrm{d}E}{\mathrm{d}Z} = \frac{\mathrm{d}\Delta E}{\mathrm{d}Z}, \tag{8}$$

which means the energy barrier applies a force on the liquid against the force resulting from the surface energy to minimize the whole energy of the system. By employing the above idea and eqs. (6) and (7), we obtained the solution for eq. (8), which is referred to as Z_{t2}. Moreover, in the case that H is close to zero, we were able to obtain a much simpler formula to estimate the penetration depth Z (see Supporting Information online). From Table 1, we can see that the value of Z_{t2} is quite close to the experimental value Z; however, the data is still scattered. How to clearly visualize the motion of the liquid-vapor menisci during their transverse motion among the pillars remains a challenge and we leave this open question for future research.

Here, we want to emphasize other features of this research. In our experiment, in order to realize the C-SP-C transition, the droplet had to be very small. We checked droplets at different volumes. However, if the volume of the droplet is too large (≥30 nL), a series of problems will arise during compression. As shown in Figure 6(a), the C-SP transition only happens when the plate is very close to the sample, i.e., H=10 μm. A big droplet with a very large transverse area will always break down to small satellite droplets. Moreover, when the pancake liquid reaches its maximum size, its width could be as large as 5 mm. This suggests that the glass plate has to be very well controlled to guarantee that it is parallel to the substrate, otherwise, the droplet will be squeezed out of the gap between the glass plate and the substrate before the C-SP transition occurs, as shown in Figure 6(b). Studying these complex phenomena in their entirety is challenging and requires extensive research that goes beyond the scope of this paper. We will leave these topics for our future studies.

4 Conclusions

In this paper, we have reported that small droplets can become suspended in micropillars under an external pressing force. In contrast to the previous reported results (such as the irreversible C-W wetting-state transition [18,37,38], the W-C

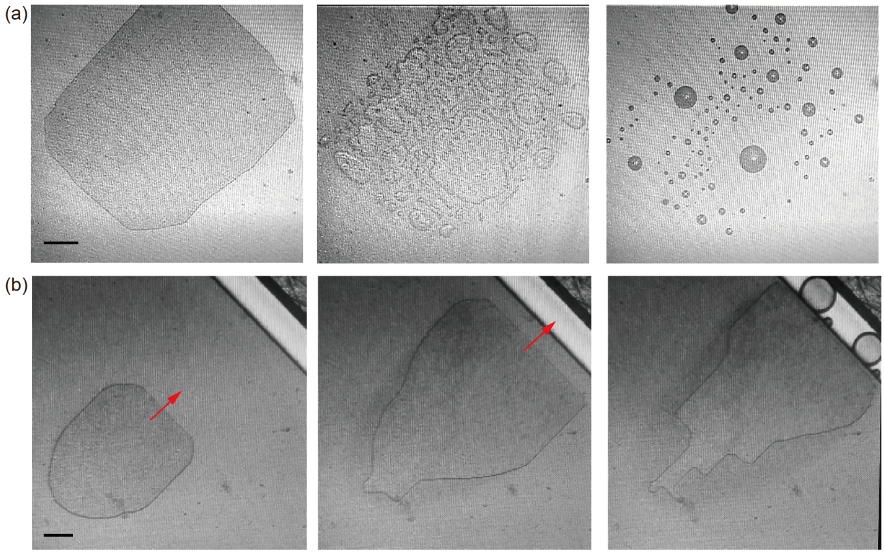

Figure 6 (Color online) Scenarios of two typical failures of the C-SP-C transition. (a) The pressing force leads to a breakdown of the Cassie-Baxter wetting state, and the main droplet breaks into many satellite droplets. (b) The droplet is squeezed out of the gap between the glass plate and the substrate. The scale bars are 1 mm.

intermediate wetting state [17,38], and the monostable CWC wetting transitions [28]), even though the micropillars were penetrated by the liquid interface of the droplet under a certain external pressure, the Cassie-Baxter wetting state was able to recover, thus avoiding a transition into the Wenzel wetting state. This wetting behavior is able to enhance the stability of the hydrophobicity. Moreover, we have constructed a simple theoretical model to determine the penetration depth of the liquid to capture the experimental results. Our experimental results suggest that the SP state could be influenced by a number of factors, such as the volume of the droplet, the contact angle hysteresis, and the contact-line pinning, which makes an accurate estimation of the relevant values quite challenging. Furthermore, some open questions remain that need to be addressed, for example, what are the criteria that account for the morphology transition from the circular shape to the square shape during compression and the transition from the Cassie-Baxter wetting state to the SP wetting state? It would be interesting to explore the dynamics of the transition, as well as the variation of the morphology of the droplet and the motion of the solid-liquid-vapor three-phase contact lines [39,40]. However, our experiments suggest that in order to guarantee the occurrence of the SP wetting state, the area fraction and the pillar height of the micropillared substrate should have large values. We expect this work will shed new light on the design of robust superhydrophobic materials and provide more novel fundamental perspectives on wetting.

This work was supported by the National Natural Science Foundation of China (Grant Nos. 11632009, and 11872227).

Supporting Information

The supporting information is available online at phys.scichina.com and http://link.springer.com/journal/11433. The supporting materials are published as submitted, without typesetting or editing. The responsibility for scientific accuracy and content remains entirely with the authors.

1 C. Neinhuis, and W. Barthlott, Ann. Bot. **79**, 667 (1997).
2 R. Blossey, Nat. Mater. **2**, 301 (2003).
3 R. Fürstner, W. Barthlott, C. Neinhuis, and P. Walzel, Langmuir **21**, 956 (2005).
4 Y. Lu, S. Sathasivam, J. Song, C. R. Crick, C. J. Carmalt, and I. P. Parkin, Science **347**, 1132 (2015).
5 X. Q. Feng, X. Gao, Z. Wu, L. Jiang, and Q. S. Zheng, Langmuir **23**, 4892 (2007).
6 D. Quéré, Annu. Rev. Mater. Res. **38**, 71 (2008).
7 C. H. Chen, Q. Cai, C. Tsai, C. L. Chen, G. Xiong, Y. Yu, and Z. Ren, Appl. Phys. Lett. **90**, 173108 (2007).
8 N. Miljkovic, R. Enright, Y. Nam, K. Lopez, N. Dou, J. Sack, and E. N. Wang, Nano Lett. **13**, 179 (2013).
9 N. Miljkovic, R. Enright, and E. N. Wang, ACS Nano **6**, 1776 (2012).
10 L. Cao, A. K. Jones, V. K. Sikka, J. Wu, and D. Gao, Langmuir **25**, 12444 (2009).
11 J. Lv, Y. Song, L. Jiang, and J. Wang, ACS Nano **8**, 3152 (2014).
12 M. J. Kreder, J. Alvarenga, P. Kim, and J. Aizenberg, Nat. Rev. Mater. **1**, 15003 (2016).
13 E. Bormashenko, R. Pogreb, G. Whyman, and M. Erlich, Langmuir **23**, 12217 (2007).
14 E. Bormashenko, R. Pogreb, G. Whyman, and M. Erlich, Langmuir **23**, 6501 (2007).
15 Y. C. Jung, and B. Bhushan, J. Microsc. **229**, 127 (2008).
16 Y. C. Jung, and B. Bhushan, Langmuir **24**, 6262 (2008).
17 Q. S. Zheng, Y. Yu, and Z. H. Zhao, Langmuir **21**, 12207 (2005).
18 P. Papadopoulos, L. Mammen, X. Deng, D. Vollmer, and H. J. Butt, Proc. Natl. Acad. Sci. USA **110**, 3254 (2013).
19 A. Lafuma, and D. Quéré, Nat. Mater. **2**, 457 (2003).
20 T. N. Krupenkin, J. A. Taylor, E. N. Wang, P. Kolodner, M. Hodes, and T. R. Salamon, Langmuir **23**, 9128 (2007).
21 R. J. Vrancken, H. Kusumaatmaja, K. Hermans, A. M. Prenen, O. Pierre-Louis, C. W. M. Bastiaansen, and D. J. Broer, Langmuir **26**, 3335 (2010).
22 J. B. Boreyko, and C. H. Chen, Phys. Rev. Lett. **103**, 174502 (2009).
23 J. B. Boreyko, C. H. Baker, C. R. Poley, and C. H. Chen, Langmuir **27**, 7502 (2011).
24 J. B. Boreyko, and C. P. Collier, J. Phys. Chem. C **117**, 18084 (2013).
25 W. Lei, Z. H. Jia, J. C. He, T. M. Cai, and G. Wang, Appl. Phys. Lett. **104**, 181601 (2014).
26 C. Dorrer, and J. Rühe, Langmuir **23**, 3820 (2007).
27 T. Mouterde, G. Lehoucq, S. Xavier, A. Checco, C. T. Black, A. Rahman, T. Midavaine, C. Clanet, and D. Quéré, Nat. Mater. **16**, 658 (2017).
28 Y. S. Li, D. Quéré, C. J. Lv, and Q. S. Zheng, Proc. Natl. Acad. Sci. USA **114**, 3387 (2017).
29 Y. P. Zhao, and Q. Yuan, Nanoscale **7**, 2561 (2015).
30 Z. Wang, and Y. P. Zhao, Phys. Fluids **29**, 067101 (2017).
31 C. Ishino, K. Okumura, and D. Quéré, Europhys. Lett. **68**, 419 (2004).
32 G. Dupeux, P. Bourrianne, Q. Magdelaine, C. Clanet, and D. Quéré, Sci. Rep. **4**, 5280 (2014).
33 I. U. Vakarelski, N. A. Patankar, J. O. Marston, D. Y. C. Chan, and S. T. Thoroddsen, Nature **489**, 274 (2012).
34 R. Maboudian, W. R. Ashurst, and C. Carraro, Sens. Actuat. A-Phys. **82**, 219 (2000).
35 C. Lee, Y. Nam, H. Lastakowski, J. I. Hur, S. Shin, A. L. Biance, C. Pirat, C. J. “CJ” Kim, and C. Ybert, Soft Matter **11**, 4592 (2015).
36 N. Vrancken, S. Sergeant, G. Vereecke, G. Doumen, F. Holsteyns, H. Terryn, S. De Gendt, and X. M. Xu, Langmuir **33**, 3601 (2017).
37 P. Wang, J. Su, M. Shen, M. Ruths, and H. Sun, Langmuir **33**, 638 (2017).
38 C. Luo, and M. Xiang, Microfluid Nanofluid **17**, 539 (2014).
39 Q. Yuan, and Y. P. Zhao, J. Fluid Mech. **716**, 171 (2013).
40 E. Chen, Q. Yuan, and Y.-P. Zhao, Soft Matter **14**, 6198 (2018).